ELECTROMAGNETIC LITHIUM RING COMPRESSION FOR MAGNETIZED TARGET FUSION APPLICATION: TRAJECTORIES

Jean-Sebastien Dick[1,*], Nick Sirmas[1,*], Scott Bernard[1], Lemuel Santos[1], Piotr Forysinski[1]

[1]General Fusion, Richmond, British Columbia, Canada

ABSTRACT

To achieve commercially relevant fusion conditions in a magnetized plasma, rapid and efficient heating must surpass heat loss. In Magnetized Target Fusion (MTF) experiments, which heat plasma by compression, a magnetic flux conserver made of metal is essential for plasma confinement, and an understanding of the compression trajectory of this plasma liner is crucial to the design and operation of the machine.

In this work, lithium rings, 527 mm in diameter and 55 mm in height, were produced by centrifugal casting and electromagnetically compressed using a high voltage power supply with capacitor energy ranging from 100 kJ to 250 kJ. High speed cameras were used to track the trajectories of the inner and outer edges of the top surface of the ring, as well as its inner edge at the equator. Magnetic field sensors were positioned at a number of radial locations to measure the change in magnetic flux density during ring compression. Ring parameters, such as thickness and temperature, were explored to attain symmetric compression trajectories free of buckles.

A 2D-axisymmetric numerical model was developed using the ANSYS LS-DYNA software package to predict compression trajectories and evaluate the energy efficiency of the compression. The aim of this work is to assess the use of concentric coil electromagnetic compression, also known as a theta-pinch, in magnetized target fusion using a solid lithium liner and to validate the LS-DYNA model. Close agreement between simulation and experiment was observed. This research contributes to advancing Magnetized Target Fusion technologies, with implications for future fusion energy applications.

Keywords: Electromagnetic compression, fusion, magnetized target fusion

1. INTRODUCTION

In December 2022, it was announced that the National Ignition Facility (NIF) achieved 3.15 MJ of fusion energy from 2.05 MJ of laser light [1]. The net energy gain was repeated another four times in six attempts over the year 2023 demonstrating that fusion ignition is not coincidental [2]. This milestone generated public interest and increased the number of private-public partnerships in the field of nuclear fusion. According to the Fusion Industry Association, there are no less than 43 private companies aiming at commercializing fusion within the next 20 years [3]. This competitive environment forces innovation and rapid prototyping of technologies that could lead to fusion energy generation. One of these technologies is Magnetized Target Fusion (MTF). MTF combines the compressional heating characteristic of inertial confinement fusion (ICF) with the reduced thermal transport and the enhanced alpha heating associated with magnetic confinement fusion (MCF) [4].

Much of the current MTF work grew out of studies on imploding liners for controlled fusion at the Kurchatov Institute of Atomic Energy [5] which inspired the Linus project at the Naval Research Laboratory [6] and later the fast-liner project at Los Alamos [7]. MTF approaches rely on the implosion of a magnetic flux conserver (liner) around a pre-heated magnetized plasma. One common challenge across these approaches is achieving a symmetrical implosion. Researchers at Los Alamos National Laboratory proposed to generate a high-density field-reversed configuration (FRC) plasma using a conical azimuthal discharge (theta-pinch) and direct it into an aluminum liner that would later be compressed using an axial discharge (Z-pinch) [8]. The idea was supported by their work on high-speed compression of aluminum liners. Radiographs presented in [9] showed excellent symmetry up to a radial compression of 13:1 for a 1-mm-thick liner with a 50 mm radius. In that experiment, the liner's inner surface velocity reached 5 km/s, considerably reducing the growth-rate of inner surface perturbations. The same group also compared the compression of liners using a Z-pinch versus a theta-pinch discharge [10]. The Z-pinch showed higher capacitor energy to kinetic energy (35%) versus 25% for the theta-pinch. However, it was mentioned that the theta-pinch allowed for easier plasma diagnostic access and better compatibility with the plasma injection system.

Instead of relying on a FRC for plasma formation, General Fusion proposes to inject a magnetized plasma generated by a coaxial plasma injector [11] into a spherical tokamak made of rotating liquid metal and a central shaft and compress it using

*Corresponding author: js.dick@generalfusion.com,
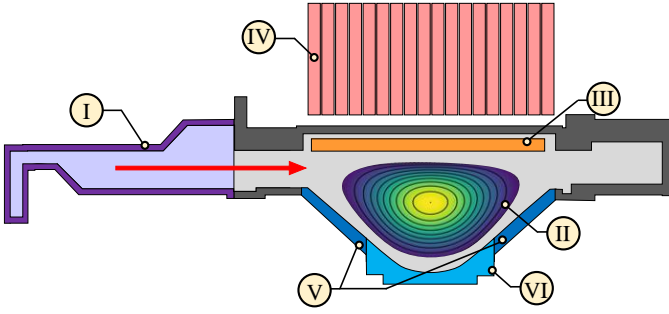nick.sirmas@generalfusion.com

FIGURE 1: Partial and simplified cross-section of LM26 machine showing the plasma injector connected to the electromagnetic compressor. I) Plasma injector, injection direction shown. II) Plasma. III) Lithium liner. IV) Concentric compression coils. V) Center cone. VI) Center shaft with diagnostic equipment.

pneumatic pistons [12]. A similar idea was sketched by Fowler at Lawrence Livermore Laboratory as the Pulsed Spheromak reactor concept [13]. By pulsing a toroidal field in the cavity, the injected plasma's initial temperature and density is increased, and its thermal confinement is improved. The flux conserver implosion velocity can be reduced compared to the liner implosions required for MTF applications using a FRC plasma. Slower implosion speeds permit the use of mechanical systems like check valves [14] or pistons that can partially recover the driving energy of a liquid metal liner. Using a water-based testbed, researchers at General Fusion demonstrated that an ellipsoidal shape suitable for plasma confinement can be achieved during implosion by spatially varying the amplitude and timing of pressure applied at the liner's outer surface [15].

Prior to building a first liquid liner MTF prototype using a mechanical compressor, General Fusion is developing an electromagnetic compressor to implode cylindrical liners made of solid lithium. The compressor will be connected to the currently operational PI-3 injector [16] which can produce plasmas of temperatures above 300 eV with an electron density of 4×10^{19} m^{-3} and thermal confinement lifetime between 5 and 10 ms [17]. The electromagnetic compressor (Fig. 1) is a theta-pinch device made of concentric coils with variable spacing connected to an 18 MJ capacitor bank. The plasma is compressed between the magnetically imploding liner and a conical conducting structure at the centre of the machine. Diagnostic ports in this central shaft will be used to detect emitted neutrons at peak plasma compression [18]. The combined machines are labeled LM26 and are planned to be operational by 2025.

The design of the LM26 machine is driven by simulation and experimental studies. Developing accurate and precise simulation tools will reduce the number of tests needed during the LM26 experimental campaign to achieve symmetrical compression and the rate of plasma heating required to achieve fusion conditions.

A testbed with two concentric coils to compress solid lithium rings was designed and constructed as a first experiment to test this electromagnetic compression scheme. The rings are 1/4 of the radius of liners expected in LM26 and can be heated up to 120 °C. The thickness of the rings can vary from 1/50th to 1/10th of their outer radius.

The experiments are reproduced using the ANSYS LS-DYNA commercial software package to capture the multi-physics of the problem. This is a common tool that has been used in electromagnetic forming problems [19–23]. The explicit structural solver is coupled to the electromagnetic solver through the addition of Lorentz forces to the mechanics equations of motion, and Ohmic heating to the structural thermal solver [19, 24]. By using the Boundary Element Method (BEM) for the surrounding air and insulators, LS-DYNA can limit computational issues related to highly deforming domains, while also capturing contacts between electrically conducting metallic parts, which is an important requirement for simulating the LM26 liner compression. Of particular interest to this study is the work by Takekoshi [22, 23], who used LS-DYNA to accurately reproduce the compression of a magnetic field from the electromagnetic compression of a copper ring. The copper ring, with an initial radius of approximately 50 mm, was compressed in less than 50 μs, smaller and faster than what is expected in the present work. Despite the differences in scale, their methodology highlights some of the capabilities and best practices in using LS-DYNA for such a problem.

The present paper compares numerical results obtained using ANSYS LS-DYNA against experimental measurements taken during lithium ring implosion tests. The objectives of the current study are to evaluate if the conversion of capacitor energy to kinetic energy is suitable for a larger MTF application, and to demonstrate that numerical simulations using LS-DYNA can accurately capture the trajectory of an imploding lithium ring.

2. EXPERIMENTAL APPARATUS

The experimental apparatus comprises four main components: a lithium ring to be compressed, compression coils used to generate the driving magnetic field, a high-voltage power supply, and diagnostic equipment to characterize the implosion.

Figure 2 shows a simplified overview of the compression equipment. A photo of the apparatus is shown in Fig. 4. The lithium ring is concentrically aligned inside the compression coils and axially centered by a thin plastic lip attached to the coil structure. The outer diameter of the lithium ring is nominally 527 mm, with an axial thickness of 50 mm and radial thickness ranging from 20-25 mm for the rings presented in this work.

The coil structure is composed of eight single-turn, flat, 6-mm-thick aluminum coils with nominal ID 539 mm, stacked to a total height of 56 mm. Adjacent coils are separated by a layer of laminated DMD® insulation to prevent arcing. The coils are structurally supported by 19-mm-thick fiberglass elements. The geometry of the single-turn coils includes optimized grooves to reduce azimuthal non-uniformities in the generated magnetic field by creating a current path that follows closely the inner perimeter of the coil while minimizing structural stress. The coils are stacked with 45-degree azimuthal clocking to further reduce localized non-uniformities. Figure 3 shows the geometry of a single coil, with a necking region on the inlet and outlet used to direct the current path.

The eight coils are electrically connected in two sets of four: the bottom four coils are connected sequentially in series to form one set, while the top four coils are similarly connected to form the second set. The power supply is composed of a bank of twenty-
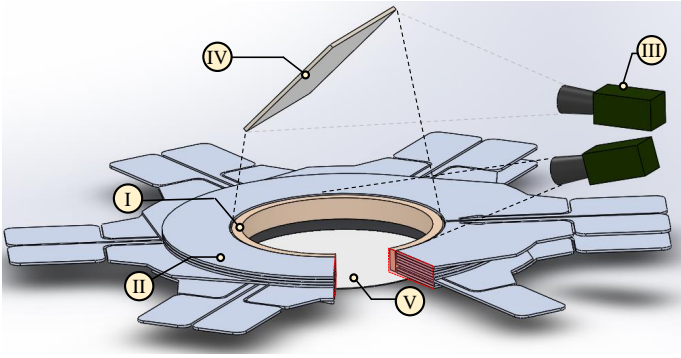
FIGURE 2: Overview of the components of the experimental apparatus. I) Lithium liner. II) Compression coils. III) High-speed cameras. IV) Mirror. V) Fiducial.
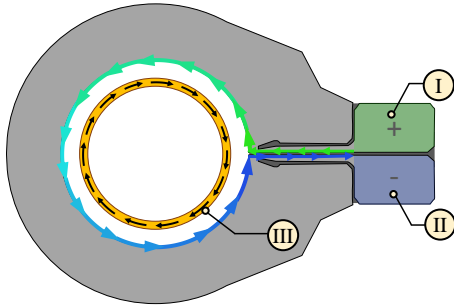

FIGURE 3: Simplified single-turn compression coil with current path shown. I) Positive electrode. II) Negative electrode. III) Lithium liner with induced current shown.

four high voltage 104 μF capacitors that are divided to supply the two sets of coils. The capacitors can operate up to 16 kV and discharged through the coils to initiate the compression.

The compression assembly is operated in air within a shipping container, to contain lithium and projectile hazards.

2.1 Lithium Rings

Lithium rings are produced using an in-house centrifugal casting apparatus. Solid lithium ingots are placed in the casting apparatus, melted, and spun about the vertical axis at speeds of approximately 500 RPM. The speed was sufficient to overcome gravitational effects and create a ring with little variation in thickness. The casting apparatus is heated to temperatures ranging from 200 °C to 240 °C. The molten lithium is pressed to the outer
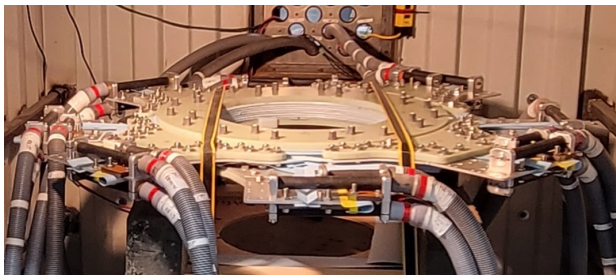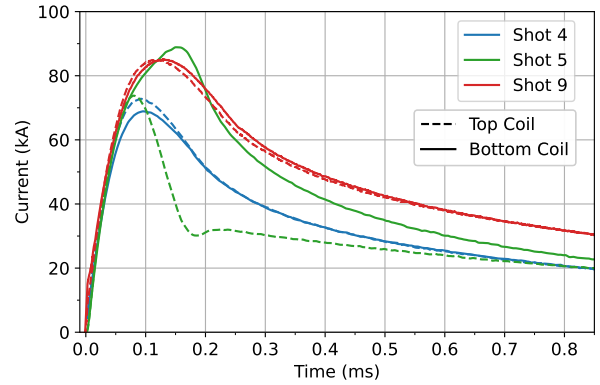

FIGURE 4: Experimental apparatus.

FIGURE 5: Currents measured in each coil taken from select test shots.

walls of the casting apparatus to form a ring, which is then cooled and solidified. A total of 11 lithium rings were cast and imploded during this experimental campaign. Three rings were chosen for the current study due to their favourable surface quality, and range of operating conditions (temperature, power supply, and available measurements) that made them ideal candidates to compare with the numerical models. Dimensional information and operating conditions for the rings that were selected for numerical model validation are presented in Table 1.

2.2 Data Collection

A pair of high-speed cameras (Photron FASTCAM Nova S12) are used to record the behavior of the lithium ring as it is compressed. Videos of liner implosions are recorded at a frame rate of 22500 frames per second. An on-axis view is obtained using a 45-degree mirror mounted above the experiment and is used to extract the liner trajectory during compression. A second off-axis view is recorded to capture, in part, the inner and outer faces of the ring. Figures 6 and 7 show stills from the on-axis and off-axis views of the implosion of ring 9, respectively.

Time varying current running through the compression coils is measured by in-house calibrated, passively integrated Rogowski coils. Measured currents for the shots of interest presented in Table 1 are shown in Fig. 5. Induced current in the lithium ring is determined using current measurements through the compression coils and a Rogowski coil encapsulating the compression coils and the lithium ring. A profile of the magnetic field surrounding the lithium ring during the implosion is obtained using measurements from an array of magnetic field probes. The magnetic field probes were designed and wound in-house using custom 3D printed coil formers and were calibrated with a known field in a 3-axis Helmholtz coil.

2.3 Calibration

A circular checkerboard pattern is used to calibrate the video to perform measurements on the liner. Each checkerboard is radially spaced by 10 mm to a maximum of 270 mm at the edge of the machine. The pattern is placed at the same height as the

TABLE 1: Shot parameters

|	Geometrical parameters			Shot conditions				
Shot	OD (mm)	Thickness (top/bottom) (mm)	Height (mm)	Temperature (°C)	Number of Caps	Voltage (kV)	Estimate cap energy (kJ)	Notes
4	527	24.9/25.4	53.4	40	20	14	203.8	
5	527	24.3/24.6	53.0	100	24	14	244.6	Partial power supply failure for top coil stack
9	527	25.6/26.2	53.9	100	24	14	244.6	
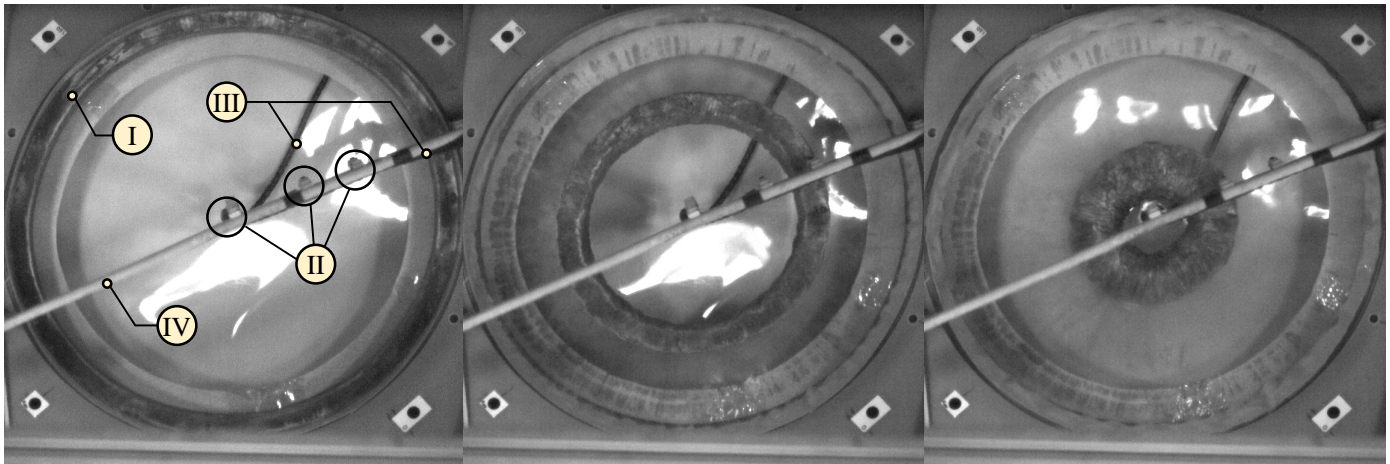
(a) $t = 0$ ms (b) $t = 0.48$ ms (c) $t = 0.75$ ms
I) Lithium liner. II) Magnetic field probes.
III) Rogowski loop.

FIGURE 6: On-axis view of implosion of lithium ring 9 as observed by the first high-speed camera.
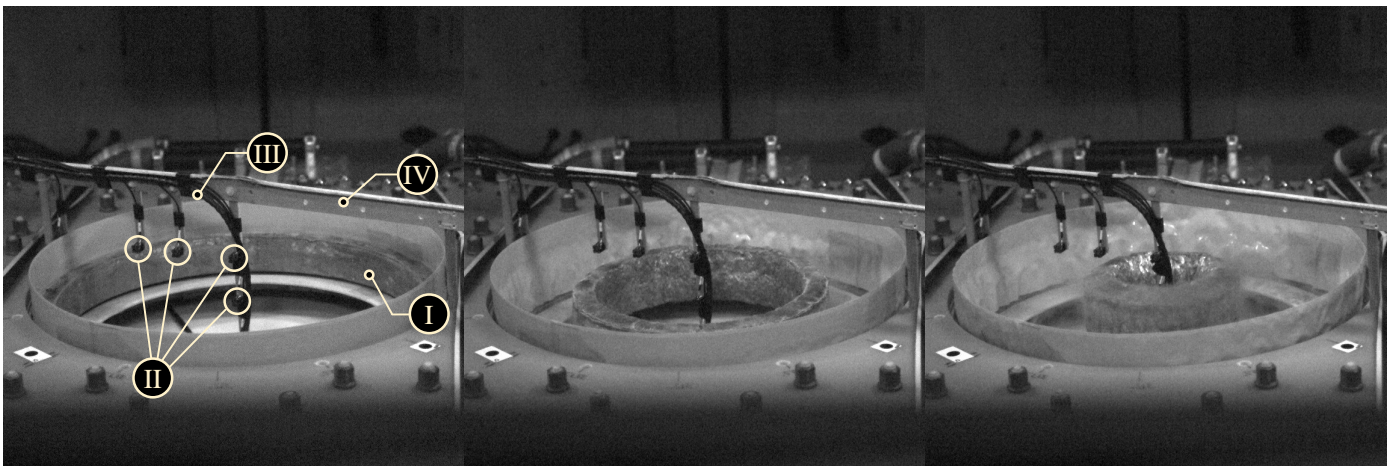
(a) $t = 0$ ms (b) $t = 0.48$ ms (c) $t = 0.75$ ms
I) Lithium liner. II) Magnetic field probes.
III) Rogowski loop. IV) Diagnostic equipment
support structure.

FIGURE 7: Off-axis view of implosion of lithium ring 9 as observed by the second high speed camera.
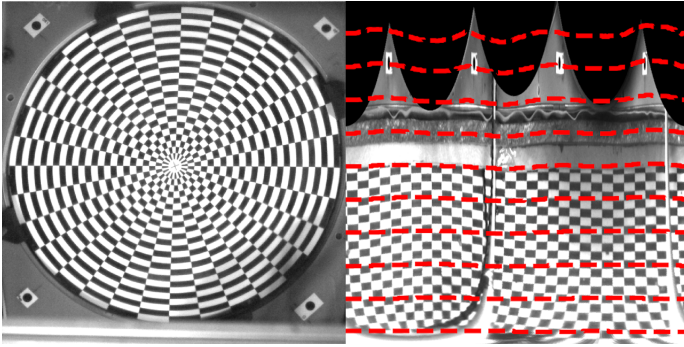
FIGURE 8: Calibration frame with checkerboard pattern (left) and calibrated polar transform with contour map (right).

FIGURE 9: Off-axis view edges (left) and liner edge extraction (right), from top to bottom: upper outer, upper inner, and equator edges.

top of the liner. The calibration aims to convert a pixel location to real-world coordinates in millimeters.

There are a few factors that can affect the accuracy of the calibration. First, the mirror used to reflect the image to the camera is not perfectly flat. Sections of the mirror are warped and distort straight edges to appear curved. In addition to the mirror, the camera lens also introduces distortion. Objects toward the outer edges of the frame experience more distortion than areas near the center of the lens.

The calibration is performed in two dimensions to account for warping induced by the mirror and lens distortion. Frames are transformed and processed in polar coordinates. The polar transformation is then sliced in axial and radial directions. The resolution of the slices is determined by the resolution of the camera (1024×1024).

At an axial slice, each extracted vertical pixel is assigned a millimeter value using the checkerboard squares as a ruler. Using the extracted vertical pixels, a polynomial fit is used to determine a pixel to millimeter function. The output of the calibration is a function to convert (x, y) pixel coordinates to (theta, r) values. Figure 8 shows a calibrated video frame transformed to polar with an overlayed contour map. Each contour is spaced approximately 35 mm apart.

2.4 Centering and Tilt Correction

The center of the liner is used to set where the radius is zero and where all extractions are measured from. The camera system is not perfectly coaxial with the center of the ring due to tilting and translation in both the camera and mirror setups. This yields a non-circular liner when viewed in the video. Figure 6 shows raw non-corrected images from the camera. The liner ring appears distorted and almost oval.

Four black circle fiducials are placed in each quadrant of the ring compressor. Figure 8 shows the four fiducials starting from the top left. The four corners are constrained to be a square, which enables to transformation of the video using homography techniques. The center of the square is used as the center of the liner for the entire shot, defined as $r = 0$ mm in polar coordinates.

2.5 Data Extraction

Extraction is performed via manual tracing using a custom Python program. Using the video, at each frame leading up to
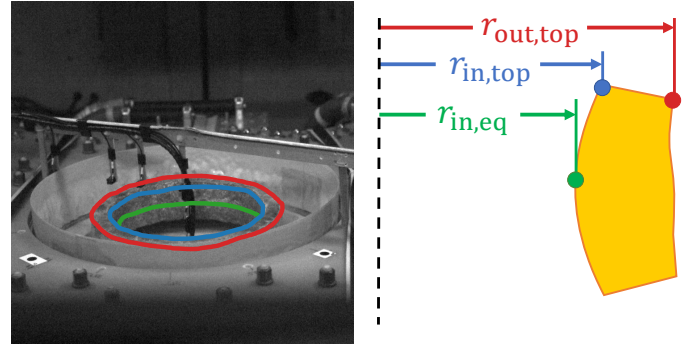
peak compression, three edges of the liner are extracted. Figure 9 shows all three liner edges: the upper inner (blue, $r_{in,top}$), upper outer (red, $r_{out,top}$), and the equator (green, $r_{in,eq}$). The center ($r = 0$ mm) is consistent throughout the video; determined from the four fiducial markers. The bottom edges of the liner were not tracked due to being occluded by the upper edges when viewed by the camera.

2.6 Extraction Errors

Liner edges are manually traced to follow the shape of the liner. The resolution and exposure of the videos are not adequate to extract finer details of the edges; blurring was often observed. Difficulties in contrast and lighting also lead to errors as the edges are not clearly defined. An uncertainty value of ± 0.7 mm was calculated taking into account the setup, calibration, and extraction errors. The uncertainty value is the standard deviation of an extraction of a machined aluminum ring with known dimensions, similar in diameter to a cast lithium ring

As the liner compresses, it starts to grow in height (axial dimension). Figure 7 shows the evolving liner shape as the shot progresses. Figure 7c shows the top edge of the liner has grown axially compared to Fig. 7a. Calibration was only performed at the height of the top edge of the pre-shot liner; any deviation in axial position of the ring's top face during compression is not corrected for.

As the liner approaches peak compression and grows axially, the extracted radii appear larger than they really are. A similar but opposite discrepancy is present in the extraction of the equator. Using measured camera calibration parameters, the error introduced by this deviation is estimated to be no more than 2.5 mm on the radius. It should be noted that the liner's axial growth is most significant at its inner radius, therefore this additional measurement error affects the extraction of the inner radius the most.

3. NUMERICAL MODEL

Ansys LS-DYNA R15 was used to solve the coupled, multiphysics dynamics of the lithium ring compressor. The setup couples the structural, thermal, and electromagnetics of the problem.
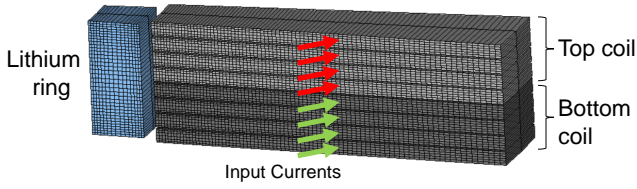
FIGURE 10: Setup of initial geometry and boundary conditions used in LS-DYNA simulation.
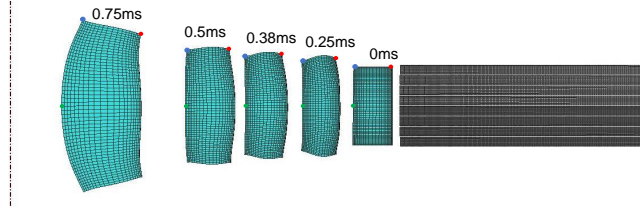

FIGURE 11: Compilation of ring compression snapshots taken at different time instances (shot 9 conditions).

3.1 Solver Setup

Simulations were conducted on a 3D geometry, shown in Figure 9, where the lithium ring and turns of each aluminum coil were represented by wedges of angle $\theta = 2\pi/64$, two cells thick. The setup represents an axisymmetric geometry where the electromagnetics are solved in 2D using the eddy current solver [20], along the mid-plane of the domain, and the structural and thermal dynamics are solved on the 3D elements.

The time history of measured currents shown in Fig. 5 are applied to each turn of the top and bottom coils, with an example of the ring dynamics shown in Fig. 11.

To best capture the transient deformations, and speed up computations, adaptive time stepping was used for the EM solver, with a maximum time step of 1.0e-6 s and minimum of 1.0e-8 s. The Finite Element Modeling (FEM) matrix was recomputed every time step. The BEM matrix was recomputed automatically based on the error calculation of the conductors' relative displacements, with a maximum of 4 time-steps between each computation. Allowing for the BEM matrix to be recomputed automatically is beneficial to speed up simulation, as this is the most time-consuming part of the EM solver.

Adaptive time stepping was also enforced for the structural and thermal solvers. A time step safety factor of 0.7 was used for the structural solver. The time step sizes for the non-linear thermal solver were set to a maximum of 1.0e-6 s and minimum of 1.0e-11 s. All simulations were performed on a single CPU on an AMD Ryzen Threadripper PRO 3995WX.

3.2 Geometry and Mesh

The dimensions of the rings used in this study were taken from Table 1 for each shot investigated, with the height, outer radius, and thickness (top/bottom) replicated. Each turn of the top and bottom coils (4 turns × 2 coils) was simplified to a
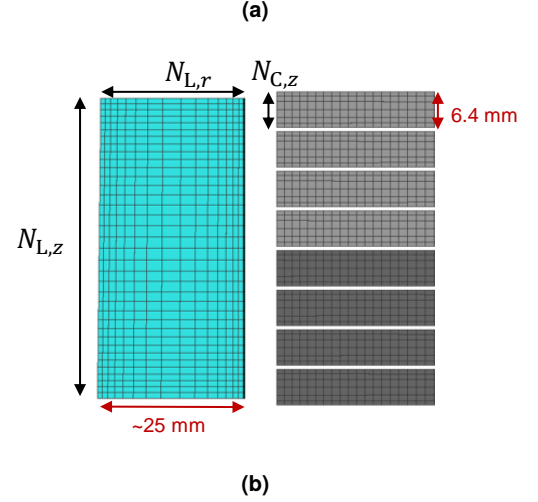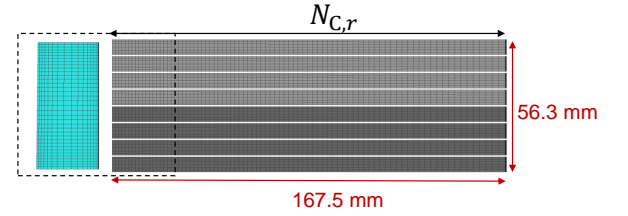

(a)

(b)

FIGURE 12: Geometry and mesh used to represent the coils and ring in simulation.

rectangular cross-section with dimensions 167.5 mm × 6.4 mm (radial × axial).

A structured mesh was created for all the conductive elements. A representation of this cross section is shown in Fig. 12. To best capture the skin depth of the conductive solid domains, element size biasing was applied towards all outer edges of the lithium ring, and the inner radius of coil turns. Details on the mesh settings used in this study are provided in Sec. 3.4.

3.3 Material Models and Parameters

The mechanical and thermal properties for the lithium ring and aluminum (6061 T6) that were used in simulations can be found in Table 2.

Linear-elastic mechanical properties were prescribed for the coils since low stress/strain was expected. For the lithium ring, a Johnson-Cook material model (Eq. 1) was used to capture the flow stress dependence on strain hardening, strain-rate hardening and thermal softening. The flow stress used in LS-DYNA is given by:

$$\sigma = \left[A + B\varepsilon_p^n\right] \left[1 + C \ln\left(\frac{\dot{\varepsilon}}{\dot{\varepsilon}_0}\right)\right] [1 - T^{*m}] \tag{1}$$

where $A, B, n, C, \dot{\varepsilon}_0$, and m are material constants, ε_p is the equivalent plastic strain, $\dot{\varepsilon}$ is the strain rate, T^* is the homologous temperature ($T^* = (T - T_{ref})/(T_{melt} - T_{ref})$). The definition of each material constant and other properties used in the study can be found in Table 2. Further details on these parameters can be found in Ref. [25].

TABLE 2: Mechanical and thermal properties

Property	Lithium	Al 6061 (T6)
Density, ρ (kg/m^3)	530	2770
Elastic Modulus, E (GPa)	7.82	71
Poisson Ratio, ν	0.48	0.33
Initial Yield, A (MPa)	0.744	-
Hardening Constant, B (MPa)	19.8	-
Hardening Exponent, n	0.3	-
Reference Strain Rate, $\dot{\varepsilon}_0$	0.002	-
Strain Rate Constant, C	0.0141	-
Thermal Softening Exponent, m	0.77	-
Melting Temperature, T_{melt} (°C)	180	-
Reference Temperature, T_{ref} (°C)	21	-
Thermal Conductivity, k (W m^{-1}°C^{-1})	84.8	114
Specific Heat, c_p (W m^{-1}°C^{-1})	3582	875

FIGURE 14: Evolution of outer (top) and inner (top and equator) ring radii over time from simulation of shot 9; comparing coarse, medium, and fine meshes.
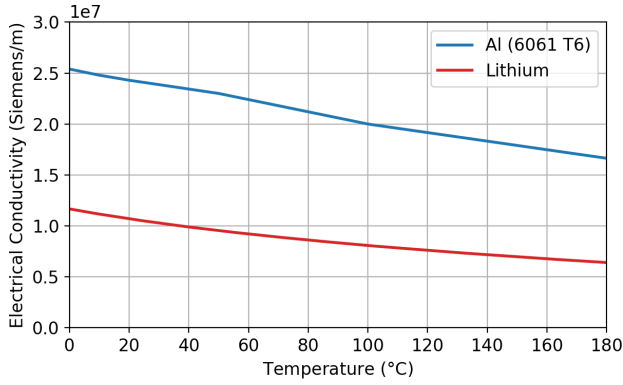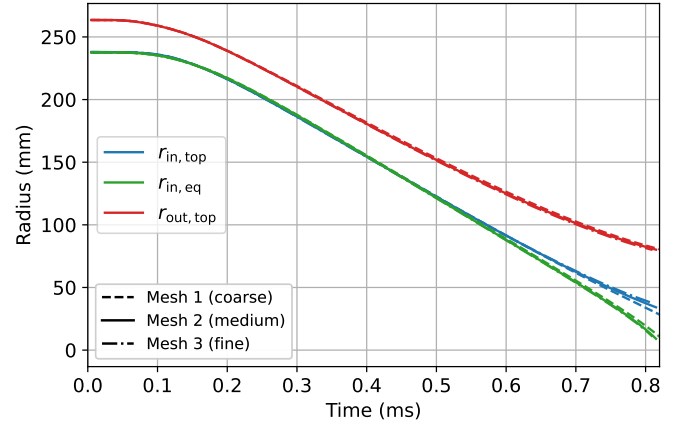

FIGURE 13: Temperature dependent electrical conductivity used in simulation for lithium and aluminum.

Lithium and aluminum (6061 T6) were assumed to have a relative permeability of 1 for this study. Figure 13 shows the temperature dependent electrical conductivities that were used in the EM solver.

3.4 Mesh Sensitivity

Three different meshes were investigated, with the discretization used for each mesh shown in Table 3 and linked to the dimensions presented in Fig. 12. Element biasing was implemented to best capture the skin depth at the inner and outer radii of the liner, and inner radius of the turns. The radial cell size at the ring edges was approximately 1.1 mm (coarse), 0.8 mm (medium), and 0.3 mm (fine). For the inner radius of the turns, these values were 3 mm (coarse), 1.4 mm (medium), and 0.7 mm (fine).

The mesh sensitivity study was completed using shot 9 from Table 1, with the corresponding currents shown in Fig. 5. An example of the ring deformation for the medium mesh is shown in Fig. 11.

The position of the liner extracted at the three locations mea-

sured in the experiment is shown in Fig. 14 for the three meshes studied. These positions were sampled at 0.8 ms and added to Table 3 with the peak amplitude of the induced current in the liner and its peak kinetic energy.

Differences between the coarse and medium mesh range from 10-20% for the different positions, while the relative difference between the medium and fine mesh range from 1% at the outer radius of the ring, and 6-8% at the inner side of the ring. Figure 14 shows that the majority of the deviation happens at very late times, when high cell distortion is observed. The difference in peak amplitude of induced currents between the coarse and the fine meshes is less than 0.5%. The difference between the peak kinetic energy is less than 0.8%. These differences are negligible considering the objectives of this study.

The elapsed times for each simulation are also shown in Table 3. Since the medium mesh captures similar behaviour to the fine mesh but with reduced computation time, this mesh was used for the remainder of the study.

4. RESULTS

Shots 4, 5, and 9, described in Table 1, were simulated using the methodology discussed in the previous section.

4.1 Liner Trajectory

The positions of the liner's edges extracted from the simulations are compared against the experimental measurements. The trajectories for shots 4, 5, and 9 are shown in Fig. 15. The azimuthal average of the measured radii is represented by the dotted line. The colored translucent bands represent the variation between the maximum and minimum measurements for a specific liner edge.

4.2 Induced Current

The current density in the r-z cross-section was integrated to compute the induced current in the liner. Figure 16 shows the time profile of the induced current from the shot 9 simulation compared to measurements obtained from the Rogowski loop (see Fig. 6a).

TABLE 3: Mesh details and performance from mesh sensitivity study

	Mesh Details					Performance					
		Coil Mesh		Ring Mesh			Radii at 0.8 ms (mm)				
Mesh	Number of Elements	Axial Elements $N_{C,z}$*	Radial Elements $N_{C,r}$**	Axial Elements $N_{L,z}$*	Radial Elements $N_{L,r}$***	Runtime	Upper Inner	Equator	Upper Outer	Peak Induced Ring Current (kA)	Peak Kinetic Energy (kJ)
M1 Coarse	3128	4	42	22	10	29 min	31.2	15.2	82.0	500	56.3
M2 Medium	9144	6	84	36	15	1h 42min	35.2	11.7	80.9	499	56.7
M3 Fine	23664	8	168	52	20	4h 17min	37.5	10.7	80.0	498	56.8

* 2:1 bias - both edges vs. mid, ** 2:1 bias - inner radius edge bias vs. outer radius, *** 4:1 bias - both edges vs. mid

TABLE 4: Key metrics between test and simulation

	Compression time (ms)		Peak Kinetic Energy (kJ)	Efficiency (%)
Shot	Test	LS-DYNA		
4	1.4	1.1	27.5	13
5	1.2	1.1	33.6	14
9	0.9	0.8	56.7	23

4.3 Magnetic Field

The B-probes shown in Fig. 6a are recreated in the simulation of shot 9. Figure 17 shows the location of the probes in the r-z plane and the contours of the simulated magnetic field at 0.14 ms. The time profile of the magnetic flux densities sampled at locations A, C, G, and J in the simulation of shot 9 are compared with experimental measurements in Fig. 18.

4.4 Compression Time and Efficiency

The compression time (CT) and the efficiency, defined as the ratio of the maximum kinetic energy over the capacitor bank initial energy, are key process indicators (KPIs) for a compression process aiming to achieve thermonuclear reaction using the MTF approach. The longer the CT, the more heat the plasma can lose to the environment. The CT is defined as the time it takes for the liner to reach its minimal radial position after the onset of its displacement. Table 4 compares CT between the simulation and the experiment and reports the efficiency based on the simulation results.

5. DISCUSSION

The following section discusses the results and proposes different hypotheses for the differences between simulation and experiment.

5.1 Input Sensitivity

The numerical simulations used experimental measurements, which carry uncertainties, as initial conditions. For example, the measured coil currents have uncertainties up to 5%. The temperature of the cast rings was measured at their outside surface just before the implosion. The lithium material model (Eq. 1) has a high coefficient for thermal softening which means that the yield strength of the material will vary significantly with small variations of temperature. Figure 19 compares simulated trajectories for three different initial temperatures for shot 9. A 20 °C variation is sufficient to cause the liner to reach a shallower or deeper compression.

This difference is more obvious when looking at the radial velocity of the liner at its equator in Fig. 20. The 120 °C liner reaches velocities up to 450 m/s while the liner initially at 80 °C reaches a peak velocity closer to only 350 m/s. Achieving, and maintaining, high velocities is necessary for reducing the growth-rate of the liner's inner surface perturbations.

5.2 Numerical Validation

An objective of this study is to evaluate the capability of the LS-DYNA model to predict the trajectory of the imploding liner.

Figure 15a shows close alignment between simulation and measurements for shot 4, however, the compression of the simulated liner stops at a radius about 25 mm greater than that measured in experiment. This may be explained by the relatively low ring temperature (40 °C) which caused the ring to show signs of azimuthal bending and large buckles in the experiment (Fig. 21a). Experimental results demonstrating a deeper compression than the 2D-axisymmetric simulation may be attributed to this buckling, which reduces the stiffness of the ring. This effect can not be captured in the current 2D-axisymmetric model and will require 3D or 2D (r-theta plane) simulations to further understand the role buckling has on the compression behaviour. It can be seen from Table 4 that the compression time is also underpredicted by the simulation, potentially due to this effect.

Shot 5 achieved one of the most azimuthally symmetric compressions out of the 11 shots performed in this campaign (Fig. 21b). The differences between the simulated and experimental trajectories (Fig. 15b) are minimal and within the uncertainty of the input parameters and the measurement process.

Shot 9 repeated the operating conditions of shot 5 without high voltage power supply failure affecting the top coil. The trajectories extracted from simulation agree with the measurements well, as seen in Fig. 15b. The compression time of the simulated shot 9 aligns with the time recorded in the experiment. The time profile of the induced azimuthal electrical current in the liner is similar between the experiment and the simulation (Fig. 16), with simulation overpredicting the peak induced current (from coils)
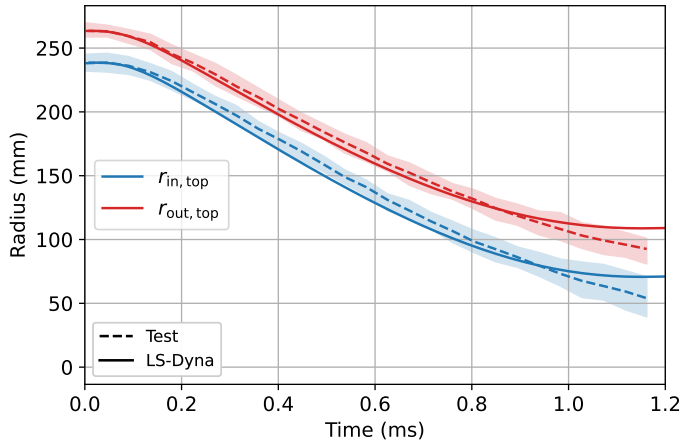
(a) Shot 4
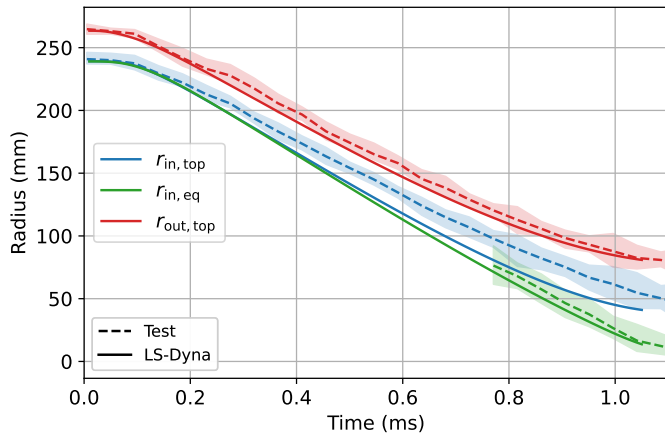
(b) Shot 5
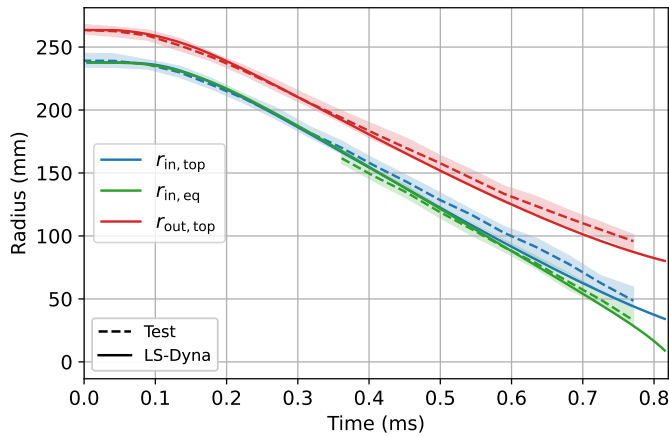
(c) Shot 9

FIGURE 15: Comparison between test and simulation for the evolution of outer (top) and inner (top and equator) ring radii over time. Transparent bands represent the range in radius measured along each circumference.
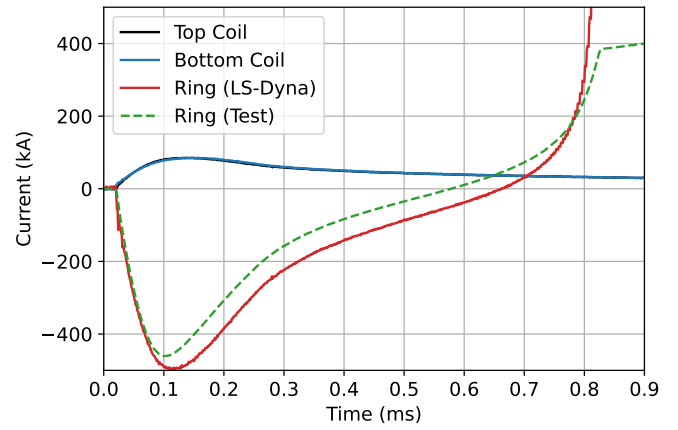

FIGURE 16: Comparison between test and simulation for the evolution of induced current within the lithium ring for shot 9. Also shown are the currents prescribed to each coil (4 turns each).

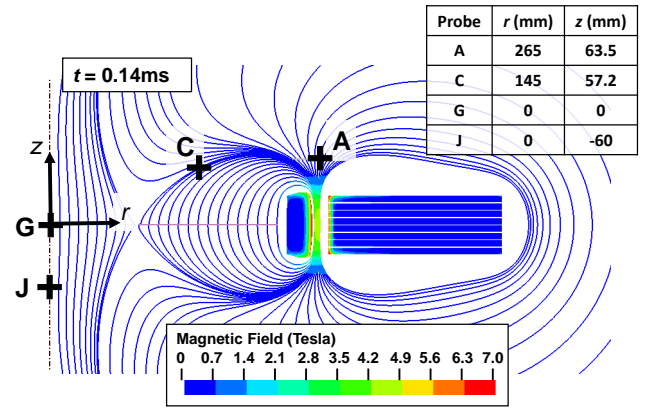| Probe	r (mm)	z (mm)
A	265	63.5
C	145	57.2
G	0	0
J	0	-60

FIGURE 17: Visual representation of the magnetic field taken from simulation for shot 9 at $t = 0.14$ ms. Probe points A, C, G, and J correspond to the probes that are present in the tests.
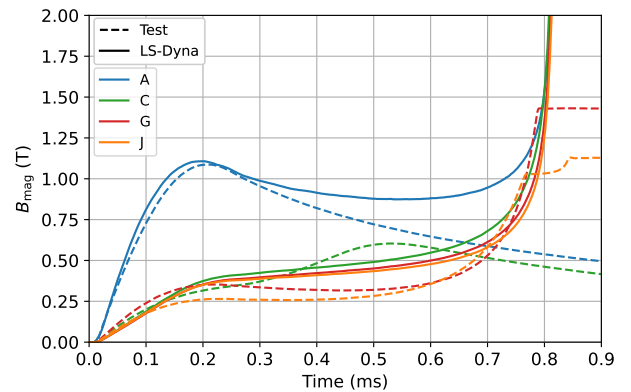

FIGURE 18: Comparison between test and simulation for the evolution of magnetic field magnitude at different probe locations, with probes corresponding to those shown in Fig. 17.
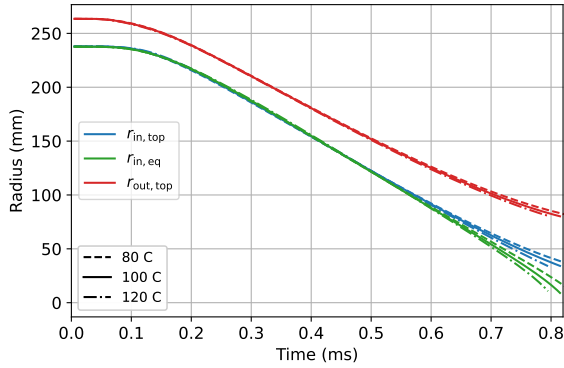
9

FIGURE 19: Evolution of outer (top) and inner (top and equator) ring radii over time, taken from simulation of shot 9 for different initial temperatures.
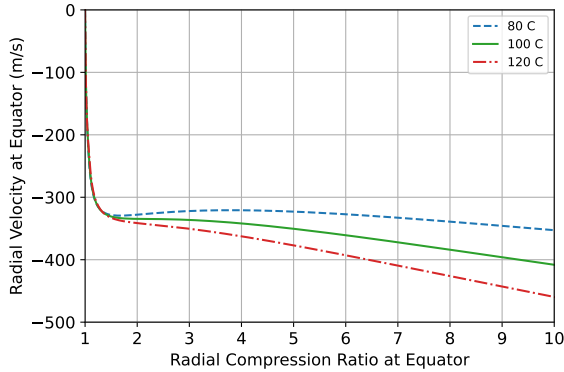

FIGURE 20: Evolution of the radial velocity at the inner radius of the ring vs the radial compression ratio (taken as $(r_{in,eq}(t = 0)/r)$) of shot 9 for different initial temperatures.

by 7%. The difference may be due the 2D-axisymmetric idealization of the ring, which shortens the current path compared to the experiment and neglects the surrounding material that may affect the magnetic field.

The magnetic field density probe data shows compression of the axial field in the readings of probes G and J, which are located at the central axis of ring, as shown in Fig. 18. The experimental probe readings stopped at peak compression near 0.8 ms. Probe A was located above the center of the gap between the ring and the compression coils. Simulation and experiment both show an initial peak magnetic field density of 1.1 Tesla at Probe A. However, the field density continues to rise in the simulation, while it decreases in the experiment. It is unclear why the simulation predicts an increase of the magnetic field density. A similar effect is seen with Probe C where the magnetic field density should be diminishing after the passage of the liner at around 0.5 ms, but the simulation predicts a rise of the magnetic field density. One possibility for this discrepancy is the idealized nature of the 2D-axisymmetric simulation, which does not include the surrounding environment or 3D nature of the coils (see Fig. 4) that may influence the magnetic field near peak compression. Another possibility might be the way LS-DYNA calculates the magnetic

(a) Shot 4   (b) Shot 5

FIGURE 21: Photographs of the compressed ring of (a) shot 4, and (b) shot 5, taken after the test.

field at a probe's location on a 2D plane. This behavior does not appear to have any impact on the trajectory of the liner.

5.3 Theta-Pinch Efficiency

The second objective of this study is to assess if a reasonable amount of capacitor bank energy can be converted into kinetic energy. This objective is relevant for the LM26 MTF campaign discussed in the introduction. Enough energy needs to be converted into kinetic energy to make the design of the LM26 high voltage power supply practical. The efficiency calculated in shot 4 was only 13%. This is likely due to the colder temperature of the liner leading to higher flow-stress. Shot 5 experienced the failure of a component in the high voltage power supply for the top coil. The calculated efficiency is not relevant as a result. Shot 9 shows an efficiency of 23% which is close to the 25% measured in the previous work of Degnan [10]. Additionally, an electromagnetically compressed ring is expected to show lower efficiency than a cylinder since the fringe magnetic field volume is relatively big compared to the near field volume, which is the region between the liner and the coil.

6. CONCLUSION

Electromagnetic compression of magnetic flux conservers made of solid lithium was achieved using a theta-pinch apparatus. The position of the liner during compression was tracked using high speed cameras. Eleven rings were compressed during the campaign, with three selected for the validation of a numerical model using the LS-DYNA EM solver. The numerical model used a Johnson-Cook material formulation with the coefficients obtained from compressive tests done by Miao [25]. Close alignment between experimental trajectories, induced currents, and magnetic field measurements with the numerical simulations confirm their capability to guide the design of MTF.

The kinetic efficiency extracted from simulation aligns with the kinetic efficiency observed in other theta-pinch experiments. From the compression shots completed, there is evidence that heating the liners to temperatures of 100 °C or above can reduce the amplitude of azimuthal buckles. Lessons learned from these ring compression experiments will be used to guide the next campaign which will look at the compression of lithium cylinders with a height greater than their radius.

REFERENCES

[1] Betti, R. "A milestone in fusion research is reached." *Nature Reviews Physics* Vol. 5 No. 1 (2023): pp. 6–8.

[2] Tollefson, J. "US nuclear-fusion lab enters new era: achieving 'ignition'over and over." *Nature* Vol. 625 No. 7993 (2024): pp. 11–12.

[3] Fusion Industry Association. *The global fusion industry in 2023*.

[4] Wurden, GA, Hsu, S C, Intrator, T P, Grabowski, TC, Degnan, JH, Domonkos, M, Turchi, PJ, Campbell, EM, Sinars, DB, Herrmann, MC et al. "Magneto-inertial fusion." *Journal of Fusion Energy* Vol. 35 (2016): pp. 69–77.

[5] Es' kov, AG, Zolotovsky, OA, Kurtmullaev, R Kh, Lauhin, Ya N, Malyutin, AJ, Markin, AJ and Semenov, VN. "Experiments on producing the plasma of high-β by longitudinal shock waves." *European Conference on Controlled Fusion and Plasma Physics*. 1973.

[6] Turchi, PJ, Cooper, AL, Ford, RD, Jenkins, DJ and Burton, RL. "Review of the NRL liner implosion program." *Megagauss Physics and Technology* (1980): pp. 375–386.

[7] Moses, RW, Krakowski, RA and Miller, RL. "Conceptual design of the Fast-Liner Reactor (FLR) for fusion power." Technical Report No. LA-7686-MS. Los Alamos National Lab.(LANL), Los Alamos, NM (United States). 1979.

[8] Schoenberg, KF and Siemon, RE. "Magnetized Target Fusion. A Proof-of-Principle Research Proposal." Technical Report No. LA-UR-99-2470. Los Alamos National Lab.(LANL), Los Alamos, NM (United States). 1998.

[9] Intrator, T, Taccetti, M, Clark, DA, Degnan, JH, Gale, D, Coffey, S, Garcia, J, Rodriguez, P, Sommars, W, Marshall, B et al. "Experimental measurements of a converging flux conserver suitable for compressing a field reversed configuration for magnetized target fusion." *Nuclear Fusion* Vol. 42 No. 2 (2002): p. 211.

[10] Degnan, JH, Turchi, PJ and Siemon, RE. "Comparison of Z-pinch and theta-pinch drive for implosion of solid liners suitable for compression of Field Reversed Configurations." *IEEE Conference Record-Abstracts. 2002 IEEE International Conference on Plasma Science (Cat. No. 02CH37340)*: p. 236. 2002. IEEE.

[11] Marshall, J. "Coaxial plasma guns as injectors of high beta linear theta pinches." *Proceedings of the High Beta Workshop*, Vol. 76. 1976. US Energy Research and Development Administration.

[12] Laberge, M. "Magnetized target fusion with a spherical tokamak." *Journal of Fusion Energy* Vol. 38 No. 1 (2019): pp. 199–203.

[13] Fowler, TK. "Pulsed spheromak reactor with adiabatic compression." Technical Report No. UCRL-ID-133884.

Lawrence Livermore National Lab.(LLNL), Livermore, CA (United States). 1999.

[14] Dick, JS, Bernard, S and Khalzov, I. "Check Valve Rotor Concept to Form an Imploding Liquid Liner for Magnetized Target Fusion Application." *Pressure Vessels and Piping Conference*, Vol. 87462: p. V003T04A023. 2023. American Society of Mechanical Engineers.

[15] Mangione, NS, Wu, H, Preston, C, Lee, AMD, Entezami, S, Ségas, R, Forysinski, PW and Suponitsky, V. "Shape manipulation of a rotating liquid liner imploded by arrays of pneumatic pistons: Experimental and numerical study." *Fusion Engineering and Design* Vol. 198 (2024): p. 114087.

[16] Epp, K, Rablah, R, Howard, S, Laberge, M, Reynolds, M, Ivanov, R, Carle, P, Young, W, Froese, A, Gutjahr, C et al. "Confinement Physics on Plasma Injector 3." *APS Division of Plasma Physics Meeting Abstracts*, Vol. 2020: pp. ZP07–011. 2020.

[17] Howard, Stephen, Zawalski, Wade, Wong, Adrian, Leci, Kathryn, Rablah, Blake, Tancetti, Andrea, Ribeiro, Celso, Carle, Patrick, Rohollahi, Akbar, Feng, Xiande et al. "Formation Efficiency Studies on the PI3 Spherical Tokamak Plasma." *APS Division of Plasma Physics Meeting*, Vol. 2023: pp. YP11–070. 2023.

[18] Braglia, F, P, Carle, Rohollahi, A, Howard, S and Hildebrand, M. "Diagnostics for the General Fusion LM26 Machine."

[19] L'Eplattenier, P, Cook, G, Ashcraft, C, Burger, M, Imbert, J and Worswick, M. "Introduction of an electromagnetism module in LS-DYNA for coupled mechanical-thermal-electromagnetic simulations." *Steel Research International* Vol. 80 No. 5 (2009): pp. 351–358.

[20] L'Eplattenier, P and Çaldichoury, I. "Recent developments in the electromagnetic module: a new 2D axi-symmetric EM solver." *Proceedings of the 10th European LS-DYNA Conference*, Vol. 2015. 2015.

[21] L'Eplattenier, P and Caldichoury, I. "A coupled 3D/2D axisymmetric method for simulating magnetic metal forming processes in LS-Dyna." *7th International Conference on High Speed Forming, April 27th-28th 2016, Dortmund, Germany*. 2016.

[22] Takekoshi, K. "Simulation of the Electromagnetic Flux Compression using LS-DYNA Multi-Physics Capability." *Proceedings of the 10th European LS-DYNA Conference 2015*. 2015.

[23] Takekoshi, K. "Study on the Electromagnetic Flux Compression using 3D Simulation." *2018 16th International Conference on Megagauss Magnetic Field Generation and Related Topics (MEGAGAUSS)*: pp. 1–7. 2018. IEEE.

[24] LSTC. *EM THEORY MANUAL - Electromagnetism and Linear Algebra in LS-DYNA* (2012).

[25] Miao, Y, Sexsmith, M, Hartono, S, Preston, C, Tsai, B and Sirmas, N. "Strain-rate-dependent parameters of lithium as a plasma facing material for magnetized target fusion application." *Pressure Vessels and Piping Conference*. 2024. American Society of Mechanical Engineers.